5-18-2019

Breakage Modeling of Needle-Shaped Particles Using The Discrete Element Method

Rohit Kumar

William Ketterhagen

Avik Sarkar

Jennifer S. Curtis

Carl Wassgren

Chemical Engineering Science: X 3 (2019) 100027

Contents lists available at ScienceDirect

Chemical Engineering Science: X

journal homepage: www.elsevier.com/locate/cesx

Breakage modeling of needle-shaped particles using the discrete element method

R. Kumar [a], W. Ketterhagen [b,1], A. Sarkar [b], J. Curtis [c], C. Wassgren [a,d,*]

[a] School of Mechanical Engineering, Purdue University, West Lafayette, IN 47907-2088, USA
[b] Worldwide Research and Development, Pfizer Inc., Groton, CT 06340, USA
[c] College of Engineering, University of California at Davis, Davis, CA 95616-5294, USA
[d] Department of Industrial and Physical Pharmacy (by courtesy), Purdue University, West Lafayette, IN 47907-2091, USA

ARTICLE INFO

Article history:
Received 20 March 2019
Received in revised form 2 May 2019
Accepted 10 May 2019

Keywords:
Particle
Attrition
Breakage
DEM
PBM

ABSTRACT

This paper models the breakage of large aspect ratio particles in an attrition cell using discrete element method (DEM) and population balance (PB) models. The particles are modeled in DEM as spherocylinders. The stresses within each particle are calculated along the particle length using beam theory and the particle breaks into two parts if the stress exceeds a critical value. Thus, the size distribution changes with time within the DEM model. The DEM model is validated against previously published experimental data.

The simulations demonstrate that particle breakage occurs primarily in front of the attrition cell blades, with the breakage rate decreasing as the particle sizes decrease. Increasing the particle elastic modulus, decreasing the particle yield strength, and increasing the attrition cell lid stress also increase the rate of breakage. Particles break most frequently at their center and the daughter size distribution normalized by the initial particle size is fit well with a Gaussian distribution. Parametric studies in which the initial particle size distribution varies demonstrate that the particle sizes approach a distribution that is independent of the initial state after a sufficient amount of work is done on the particle bed. A correlation for the specific breakage rate is developed from the DEM simulations and used within a PB model along with the daughter size distribution fit. The PB model also clearly shows that the particle size distribution becomes independent of the initial size distribution and after a sufficiently long time, is fit well with a log-normal distribution.

1. Introduction

The physical properties of an active pharmaceutical ingredient (API) are determined to a large degree by the API's particle size distribution (PSD). Changes in the PSD during manufacturing can lead to unwanted powder behavior and impact the drug product quality. While a desirable PSD can be obtained through a carefully designed crystallization process, subsequent unit operations, such as agitated filter drying, can cause an uncontrolled change in the PSD due to particle breakage and degradation (Lekhal et al., 2004; Lekhal et al., 2004). Compounding the issue, API crystals are frequently needle-shaped (MacLeod and Muller, 2012; MacLeod and Muller, 2012), which increases their probability of breakage (Hua et al., 2015; Hua et al., 2015). Thus, predicting and controlling the breakage of needle-shaped API particles during processing is an important issue for the pharmaceutical industry.

Experimental studies on this topic have been successful at predicting the overall bulk behavior, but give little information on particle-level dynamics. Particle-level information, which can be obtained from computational models, is essential for properly understanding the breakage phenomenon. In this article a discrete element method (DEM) breakage model is developed for high aspect ratio, needle-shaped particles modeled using spherocylinders. This model is applied to an agitation cell geometry to examine the effects of initial particle aspect ratio, material properties, and operating conditions on the PSD, internal particle stresses, location of breakage events, and specific particle breakage rates and resulting daughter particle size distributions. A simple population balance model is also proposed using the DEM-measured information to predict the PSD for extended run times.

* Corresponding author at: School of Mechanical Engineering, Purdue University, West Lafayette, IN 47907-2088, USA.
E-mail address: wassgren@purdue.edu (C. Wassgren).
[1] Present address: AbbVie Inc., 1 N Waukegan Road, North Chicago, IL 60064, USA.

https://doi.org/10.1016/j.cesx.2019.100027
2590-1400/

2. Background

2.1. Experimental attrition studies

A number of experimental studies have been performed to predict particle size reduction due to attrition or particle breakage in a cylindrical agitated cell. Lekhal et al. (2003, 2004) investigated the mean particle size reduction within an agitated filter dryer (AFD) for cubic crystals of KCl and needle-shaped crystals of L-threonine. They found that particle size reduction only became significant when the material was nearly dry. They also observed that the particle size approached a constant value after a large time as crystals became sufficiently small and the applied loads were no longer sufficient to continue breakage.

Using an industrial-scale AFD to perform experiments can be both expensive and tedious. In addition, traditional lab scale drying equipment has been unsuccessful in producing the same attrition and agglomeration behavior as an AFD since the stresses experienced by the material are an order of magnitude smaller at the lab scale. Lamberto et al. (2011) overcame this limitation by using a small agitation cell with a load applied on the particle bed to mimic the weight of overlying material. They utilized the reduction in the mean particle size to characterize attrition sensitivity and ranked materials as being hard, medium, or easy to break. This classification was then used as a guide to predict attrition at larger scales. AmEnde et al. (2013) used a similar experimental setup to rank material breakage propensity and examined the effects of operating parameters on particle attrition. Remy et al. (2015) built on these studies and described a new methodology to examine the degree of attrition during scale-up. Remy et al. reported that particle attrition of wet API powders was significantly smaller than what was observed for dry powders. They also observed that the mean particle size correlates well with the work done by the impeller blade on the powder bed.

In addition to an agitation cell, previous studies have also utilized shear cells to investigate multi-particle attrition. Neil and Bridgwater (1994) and Ghadiri et al. (2000) related the extent of attrition to the applied normal stress and shear strain while Potapov and Campbell (1997) proposed a relationship between the extent of attrition and the work done on the sheared particle assembly.

2.2. Computational attrition studies

DEM computational modeling has been a popular tool for studying particle breakage. However, most previous studies have used spherical particles instead of using more realistic particle shapes in order to reduce the computational time required for complex particle contact detection. Hare et al. (2011) introduced a combined DEM and experimental approach for predicting the extent of breakage in agitated particle beds using spherical particles. They combined their DEM normal stresses and shear strains with the correlation of Neil and Bridgwater (1994) to predict the extent of attrition within the bed. In this study, actual particle breakage was not considered directly in the DEM model and, thus, can only be applied to systems with a small amount of breakage since the DEM model did not account for changes in particle bed behavior due to changes in the PSD.

DEM simulations that do incorporate complex shapes generally utilize a bonded-sphere approach, which provides the flexibility to generate a wide variety of particle shapes and exploits simple sphere-sphere contact detection. However, the bonding of individual spheres causes artificially rough particle surfaces (Guo et al., 2012), smaller coefficients of restitution (Kodam et al., 2009), and increased computational costs. Grof et al. (2007) and Grof et al. (2011) used a combined DEM and population balance modeling (PBM) approach to study the breakage of needle-shaped particles modeled using the bonded-sphere method. They observed that particle breakage generally occurred at the mid-point of the needle-shaped particles, regardless of their aspect ratio. Guo et al. (2017) used a flexible bonded-sphere model to predict the breakage of needle-shaped particles in an agitation cell. They found that the particle breakage rate increased as the applied lid pressure, impeller rotational speed, particle-particle friction, and particle-wall friction increased. They also observed that the extent of breakage per impeller revolution was independent of the impeller rotational speed and breakage was a function of the work performed on the particle bed. This latter finding is consistent with the previous experimental observation by Remy et al., 2015.

Another geometry that is utilized to model needle-shaped particles is the sphero-cylinder, shown in Fig. 1. This shape consists of a cylinder with two hemispherical caps at the ends, which simplifies contact detection as there are no sharp edges to address. Several DEM studies have utilized sphero-cylinders to model needle-shaped particles for various applications (Pournin et al., 2005; Hua et al., 2013; Langston et al., 2015; Kumar et al., 2018). In their DEM study, Hua et al. (2015) utilized sphero-cylinders to calculate the internal load and moment distributions within needle-shaped particles in a vertical axis mixer. They observed that the maximum internal particle stress occurs along the particle circumference at the mid-plane, indicating that needle-shaped particles are more prone to breakage at their center. Actual particle breakage, however, was not considered in their study. Therefore, changes to the loading state of particles as the PSD changes was not examined.

In this article, a DEM breakage model is proposed for needle-shaped particles using smooth sphero-cylinders. A breakage criterion is implemented such that the particle breaks at the point where the tensile or shear stress exceeds the material yield strength. The breakage model is validated by comparing simulation and published experimental results for the breakage of chalk sticks in a cylindrical uni-axial compression cell. The breakage model is then used to predict the breakage of needle-shaped particles in an agitation cell. The influences of particle initial aspect ratio, lid stress, blade rotational speed, particle yield strength, and particle elastic modulus on the resulting particle aspect ratio, internal particle stress, breakage event location, particle breakage rates, and daughter particle length distributions are examined. Lastly, a population balance model is used to predict particle aspect ratio distributions for longer run times.

3. DEM model description

An in-house DEM code is developed to predict the dynamics and breakage of large aspect ratio particles. The DEM simulation visualization is done in OVITO v2.9 (Stukowski, 2009). This section describes the important aspects of this model, including the force models, particle breakage criteria, model validation, the population balance model (PBM), and system geometry.

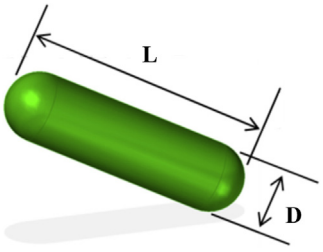

Fig. 1. Schematic of a sphero-cylindrical particle of length *L* and diameter *D*.

3.1. Force models

The contact force depends on the local geometry of the contact. There are two approaches for incorporating the contact geometry that have been proposed: (i) using a force model that is a function of the overlap volume (Nassauer and Kuna, 2013), and (ii) using a force model that is a function of the contact area (Kumar et al., 2018). From a comprehensive investigation of the influence of force models on various aspects of DEM modeling, it is revealed that for cohesionless sphero-cylinders a simplistic model, such as the Hertzian force model, can be used for force calculations (Kumar et al., 2018). The DEM Hertzian elastic normal force (Johnson, 1985) coupled with a nonlinear dissipative model (Tsuji et al., 1992) is used to calculate the normal force for particle-particle and particle-boundary interactions. The DEM normal force is calculated using,

$$F_n = k_n \delta_n^{3/2} + b_n \dot{\delta_n} \delta_n^{1/4} \tag{1}$$

where δ_n is the maximum contact overlap, $k_n = \frac{4}{3} E_{eq} \sqrt{R_{eq}}$ is a stiffness constant, $b_n = -\log(\varepsilon) \sqrt{\frac{5 k_n M_{eq}}{(\log(\varepsilon))^2 + \pi^2}}$ is a dissipation constant with ε being the coefficient of restitution, and $\dot{\delta_n}$ is the relative velocity in the normal direction of the contact. The equivalent elastic modulus is $E_{eq} = \left[\frac{(1 - \nu_1^2)}{E_1} + \frac{(1 - \nu_2^2)}{E_2}\right]^{-1}$ where E and ν are the elastic modulus and Poisson's ratio, $R_{eq} = \frac{R_1 R_2}{R_1 + R_2}$ is the equivalent radius with R being the particle hemisphere radius, and $M_{eq} = \frac{M_1 M_2}{M_1 + M_2}$ is the equivalent mass with M being the particle mass. The subscripts 1 and 2 refer to the two particles (or boundary) in contact.

The DEM tangential force is based on Mindlin-Deresiewicz theory (Mindlin and Deresiewicz, 1953; Thornton and Yin, 1991). When the tangential force exceeds Coulomb's friction force ($\mu |F_n|$), sliding friction occurs, where μ is the sliding friction coefficient and F_n is the instantaneous normal force. The DEM tangential force is calculated as,

$$F_t = k_t \delta_n^{1/2} \delta_t + b_t \dot{\delta_t} \delta_n^{1/4} \tag{2}$$

where δ_t is the relative tangential displacement, $k_t = 8 G_{eq} \sqrt{R_{eq}}$ is a stiffness constant with effective shear modulus $G_{eq} = \left[\frac{(2 - \nu_1)}{G_1} + \frac{(2 - \nu_2)}{G_2}\right]^{-1}$ where G is the particle shear modulus, $b_t = -\log(\varepsilon) \sqrt{\frac{(10/3) k_t M_{eq}}{(\log(\varepsilon))^2 + \pi^2}}$ is a dissipation constant, and $\dot{\delta_t}$ is the relative velocity in the tangential direction of the contact.

3.2. Particle breakage criterion

There are two important breakage mechanisms: (i) chipping, where small pieces are chipped off the particle's edges and surfaces, and (ii) fragmentation, where the larger particles are cleaved into smaller pieces. Prior studies (MacLeod and Muller, 2012; Remy et al., 2015) have observed that in agitated systems, fragmentation is the main breakage mechanism for large aspect ratio, needle-shaped particles.

In this work, sphero-cylinders are used to model needle-shaped particles and fragmentation is the particle breakage mechanism. Fig. 2a shows multiple imaginary breakage planes perpendicular to the particle axis. The forces and moments on an *ith* internal breakage plane segmenting a particle (Fig. 2b) are calculated utilizing Newton's second law and Euler's equation of motion, as described by Hua et al. (2015). The forces and moments on the other segment of the breakage plane are equal and opposite in sign to the first segment according to Newton's third law (Fig. 2c). For a beam with circular cross-section of radius R, the relations

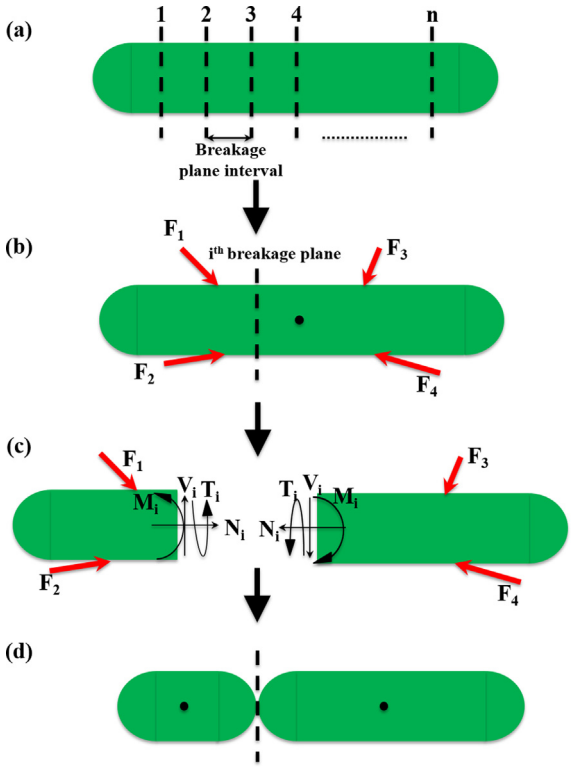

Fig. 2. Particle breakage methodology: (a) multiple imaginary breakage planes within the particle at which the particle can break; (b) a general *ith* breakage plane out of *n* breakage planes; (c) the forces and moments acting on the breakage plane, which are calculated using the algorithm described by Hua et al. (2015); (d) two daughter sphero-cylinders resulting from the breakage of a parent sphero-cylinder.

(Hibbeler, 2005) for the magnitudes of the normal stress, σ_i, and shear stress, τ_i at the *ith* breakage plane are,

$$\sigma_i = \frac{\mathbf{N_i}}{A_{cs}} + \frac{|\mathbf{M_i}| R}{I}, \sigma^{max} = max(\sigma_i) \tag{3}$$

$$\tau_i = \frac{4 |\mathbf{V_i}|}{3 A_{cs}} + \frac{|\mathbf{T_i}| R}{I_p}, \tau^{max} = max(\tau_i) \tag{4}$$

where $\mathbf{N_i}$ is the normal force, $\mathbf{M_i}$ is the bending moment, $\mathbf{V_i}$ is the shear force, $\mathbf{T_i}$ is the twisting moment, $A_{cs} = \pi R^2$ is the particle cross-sectional area, R is the particle radius, $I = \pi R^4/4$ is the area moment of inertia, and $I_p = \pi R^4/2$ is the polar moment of inertia (Fig. 2c). The particle breaks at the breakage plane where the maximum normal stress, σ^{max}, or the maximum shear stress, τ^{max}, exceeds the corresponding tensile strength or shear strength, as is illustrated in Fig. 2d. In this study, it was observed that the probability of a particle breaking simultaneously at multiple breakage planes is very small ($< 1\%$). Thus, for simplicity, a particle is allowed to break only at one breakage plane, i.e., at a given time instance a particle can break only into two pieces. In the scenario where the yield normal/shear stress is exceeded at more than one plane at a given time instance, the breakage occurs at the plane with the largest stress (normal/shear) magnitude. Note that when a sphero-cylinder breaks, the sharp breakage ends are capped with hemispheres such that the resulting daughter particles are also sphero-cylinders, as shown in Fig. 2d. As a result of this capping, there is a small mass loss ($< 3\%$ of the initial mass) at the breakage plane for particles with an aspect ratio of ten or larger. The mass loss due to capping is assumed to result in the production of fines that would percolate through the bed and have little impact on the flow behavior of the remaining particles. In case of very high

attrition rates there will be more fines generation and this could reduce the flowability of the material. However, this phenomenon is out of scope of this study, as the systems considered here have low attrition rates.

A single particle, three-point bending test was performed to verify the breakage model (Fig. 3a). In this figure, F_c is the applied force and l_h is the distance between the point of application of the applied force and the support of the three-point bending setup. A comparison of the dimensionless bending moments between the simulation and the analytical solution (Popov, 1999) at different breakage planes is shown in Fig. 3b. The numerical bending moments match well against the analytical bending moments. Although not shown here, the shear force at different cutting planes also matched well with the analytical results.

An optimal number of breakage planes should be used so that the DEM results are independent of the number of breakage planes while the simulations run in reasonable computational times. To examine the effect of the number of breakage planes, DEM simulations of uni-axial compression in a cylindrical container were performed. A uni-axial compression setup was chosen for this study since the same system was used for the model validation in which chalk sticks are compressed in a cylinderical cell, as explained in Section 3.3. Fig. 4a and b show snapshots from the uni-axial compression simulation before and after compression, respectively. The simulation parameters and material properties used in these DEM simulations are listed in Table 1. These parameters were chosen so that they match with the experiments (Section 3.3) used for the model validation. The load on the lid and the resulting daughter particle length distributions are compared for different numbers of breakage planes. Fig. 5a plots the load on top of the particle bed for the different number of breakage planes. The loading curve for unbreakable particles (zero breakage planes) is significantly larger than the breakable cases, which are insensitive to the number of breakage planes and are identical to each other. The daughter particle length distributions are plotted after a lid displacement of 70 mm, to match the displacement in the validation experiments. The distributions of the daughter particle length to initial particle length collapse over each other if the breakage plane interval is less than or equal to the particle diameter, as can be seen in Fig. 5b. Therefore, in all of the remaining DEM simulations performed for this study, the distance between breakage planes used within a particle is set equal to the particle radius.

Table 1
The parameters used in the validation simulations and their values.

Parameter	Values
Particle length, L	80 10^{-3} m
Particle diameter, D	10 10^{-3} m
Particle aspect ratio, $AR = L/D$	8
Particle density, ρ_p	1570 kg/m^3
Cylinder diameter, D_c	0.20 m
Particle elastic modulus, E_p	527.6 10^6 Pa
Particle Poissons ratio, ν_p	0.30
Boundary elastic modulus, E_b	1.0 10^9 Pa
Boundary Poissons ratio, ν_b	0.30
Particle-particle sliding friction coefficient, μ_{pp}	0.624
Particle-cylindrical boundary sliding friction coefficient, μ_{pc}	0.35
Particle-flat boundary sliding friction coefficient, μ_{pf}	0.40
Particle-particle coefficient of restitution, ε_{pp}	0.95
Particle-boundary coefficient of restitution, ε_{pb}	0.90
Particle yield strength, σ_Y	3.99 10^6 Pa

3.3. DEM breakage model validation

The DEM breakage model was validated by comparing uni-axial compression experiment results and DEM predictions. Snapshots

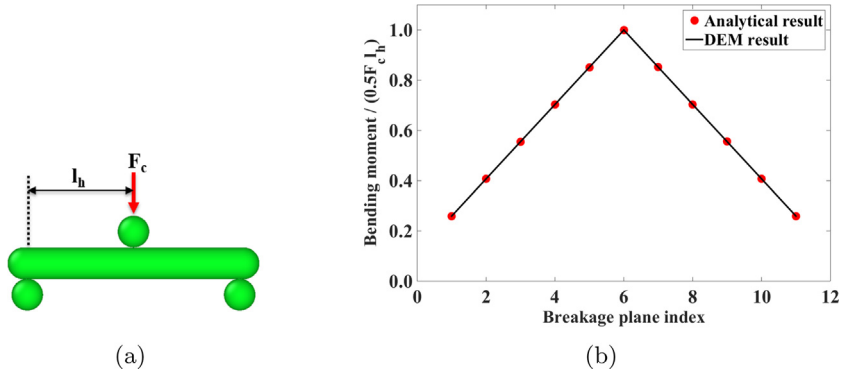

Fig. 3. Three-point bending test to verify the particle breakage model: (a) front-view of the three-point bending test on a sphero-cylinder; (b) comparison of dimensionless bending moment between the simulation and analytical beam bending relations (Popov, 1999) at different breakage planes.

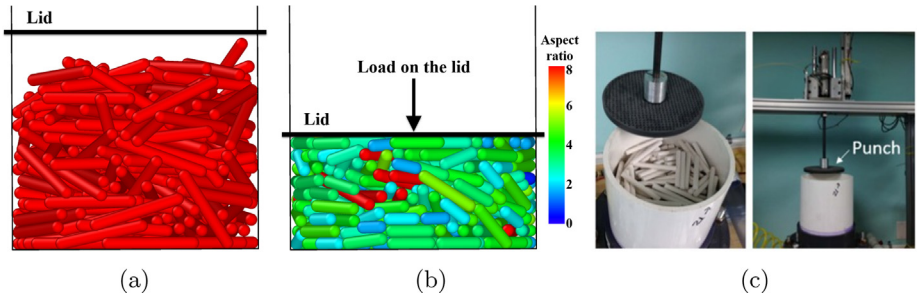

Fig. 4. Uni-axial compression in a cylindrical container: (a) a snapshot from the DEM simulation before compression; (b) a snapshot from the DEM simulation after compression with the particles colored according to their aspect ratio (red = maximum aspect ratio and blue = the minimum aspect ratio); (c) experimental uni-axial compression test performed by Guo et al. (2017). (For interpretation of the references to colour in this figure legend, the reader is referred to the web version of this article.)

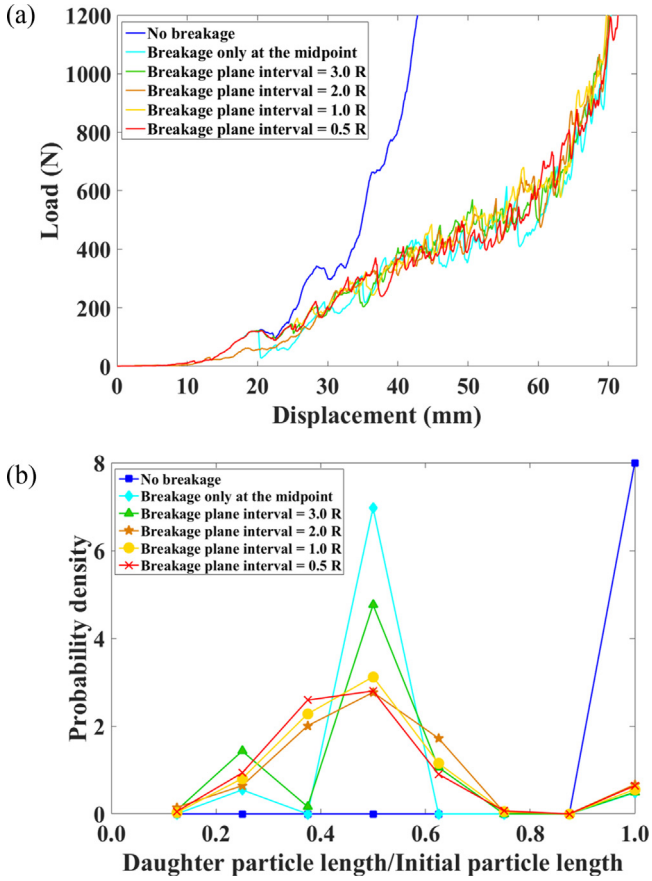

Fig. 5. DEM simulation of uni-axial compression to find the optimal number of breakage planes: (a) load applied on the top of the particle bed as a function of lid displacement for different breakage plane intervals; (b) distributions of daughter particle length to initial particle length corresponding to the lid displacement of 70 mm for different breakage plane intervals.

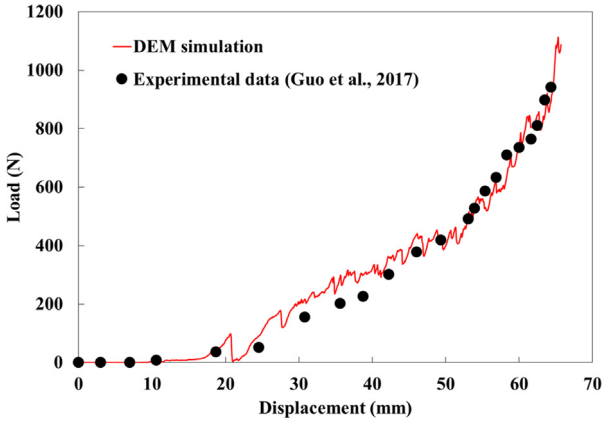

Fig. 6. Comparison between simulation predictions and the experimental results of the load applied to the top of the particle bed as a function of lid displacement.

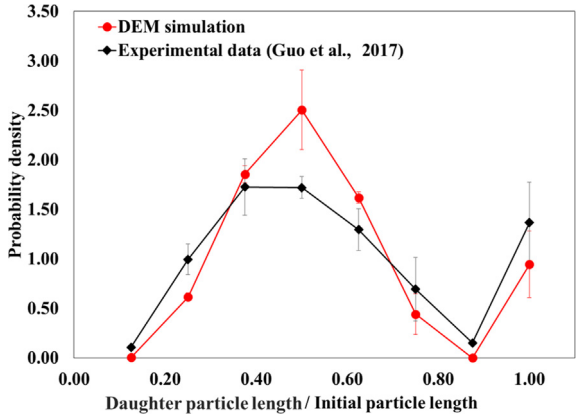

Fig. 7. Comparison of the daughter particle length distributions between the simulation and the experiment, corresponding to a load of 1025 N. The scatter bars represent one standard deviation obtained from five simulations and three experiments with different initial configurations of the particle bed.

of the uni-axial test DEM simulation before and after compression are shown in Fig. 4a and b, respectively. The uni-axial compression experiment, performed by Guo et al. (2017), is shown in Fig. 4c. The experiment is performed using 300 identical, cylindrical blackboard chalk sticks. The simulation parameters and the measured material properties are provided in Table 1. The DEM simulations follow the same procedure as the experiments. Particles are first generated at random positions with random orientation and are gently allowed to deposit under gravity. The particle bed is then slowly compressed using a lid moving downwards at a constant speed.

The load applied on top of the particle bed is plotted as a function of the displacement of the lid in Fig. 6. In the loading process, the load is increased to 1025 N by moving the lid downward at a constant speed. The loading values obtained from the DEM simulation are in good agreement with the experiment. A comparison between the daughter length distribution obtained from the simulation and the experiment under a compression load of 1025 N is given in Fig. 7. The scatter bars in the plot are obtained by repeating the simulation five times with different initial particle spatial and orientation configurations. The distribution of the daughter particle length to initial particle length has a mode occurring at 0.5, indicating that the particles are most likely to break at their midpoint. This result has been observed in previous work (Grof et al., 2007; Hua et al., 2015; Guo et al., 2017). The distributions obtained from the simulation and the experiment look similar, although the simulations overpredict the number of breakage events at the midpoint. The difference in the results is attributed to the presence of small air pockets in the chalk that can result in heterogeneous material properties (Thakur et al., 2017) and increased breakage at non-midpoint locations.

3.4. Population balance modeling

Population balance modeling can be used as a tool to predict the particle breakage in large-scale systems by utilizing particle breakage information from small-scale DEM simulations or experiments. The rate of change of particle mass in a given particle size class due to breakage can be determined using a population balance model (Rhodes, 2008). In this study, the size class refers to the parent particle aspect ratio. The rate of mass change in the size class i can be expressed in terms of the rate of change of particle number as,

$$\frac{dN_i(t)}{dt} = -S_i N_i(t) + \sum_{j=1}^{i-1} b_{ij} S_j N_j(t) \tag{5}$$

where N_i is the number of particles of size class i, particle specific breakage rate S_i is the probability of a particle of size i being broken in unit time, and the daughter distribution function b_{ij} is the fraction of breakage products from size class $j > i$ that fall into size class i. The first term on the right hand side of Eq. (5) represents the death term, which is the rate at which particles of size class i break. The second term represents the birth term, which is the generation rate of particles in size class i due to breakage of larger particles of size class

$j > i$. Population balance modeling has been widely employed to predict the breakage of large aspect ratio needle-shaped crystals. Sato et al. (2008) developed a two-dimensional (considering particle width and length) population balance model for their experiments to predict the breakage of large aspect ratio needle-shaped crystals in an agitated bed. Grof et al. (2011) developed a population balance model and utilized combined computational and experimental methods to determine the specific breakage rates and daughter distribution functions to predict the breakage of needle-shaped crystals undergoing uni-axial compression.

The parameters S_i and b_{ij} are generally assumed to be constants in PB models. However, in this study, as there is actual particle breakage implemented within the DEM code, the time-dependent values of parameters S_i and b_{ij} are readily available from the DEM simulations. The specific breakage rate S_i is expressed as,

$$S_i = \Delta N_i / (N_i \Delta t) \tag{6}$$

and the daughter distribution function b_{ij} is expressed as,

$$b_{ij} = D_{ij} / \sum_{k=1}^{j/2} D_{kj} \tag{7}$$

where D_{ij} is the number of breakage events from size class j into size class i. For binary breakage, in which two daughters are generated from one parent particle, the daughter distributions functions are normalized to two (Grof et al., 2011), such that $\sum_{i=1}^{j} b_{i,j} = 2$.

3.5. System geometry

In this study, an agitation cell similar to the one proposed by Lamberto et al. (2011) and Remy et al. (2015) is used. The modeled agitation cell consists of a cylindrical container, an impeller comprised of two vertical, flat blades and a shaft, and a lid with a prescribed load pressing downward on the particle bed to account for the overlying material weight in real operations. Initially, a number of particles with a given aspect ratio distribution are generated with random spatial positions and orientation within the agitation cell. The particles settle under gravity, after which the bed is compressed by applying a fixed load on the top lid. The particle bed is then agitated by rotating the blades about the central shaft at a constant rotational speed. Particles are allowed to break only after a steady state is attained in the particle bed, which generally occurs after two blade revolutions. The DEM simulations of the agitation cell before and after agitation are shown in Fig. 8a and b, respectively.

4. Dimensional analysis

The DEM simulations were used to investigate how the operating conditions and material properties affect particle breakage in the agitation cell. To reduce the number of parameters required for study, a dimensional analysis was performed and is described in this section.

The simulation dimensional parameters are listed in Table 2. There are 19 dimensional parameters and three reference dimensions (mass, length, and time), so according to the Buckingham-Pi theorem, there are 16 dimensionless parameters that describe the system. The set of 16 dimensionless parameters selected here is given in Table 3.

Particle breakage is caused by stresses developed within a particle resulting from particle-particle or particle-boundary interactions. The measured particle stress, σ_p, made dimensionless by the particle yield strength, σ_Y, is a function, in general, of all of the dimensionless parameters listed in Table 3. However, a full factorial study of all 16 parameters is impractical. Instead, insight from previous work can help to reduce the number of parameters that must be investigated to determine the functional dependence. For example, Freireich et al. (2009) found that the coefficient of restitution has little influence on the flow kinematics in dense granular flows. Similarly, the Froude number has been found to be unimportant at the small values usually encountered in an agitation cell (Hua et al., 2013). The Poisson's ratio is embedded in the effective elastic modulus and, thus, is unimportant by itself and can be eliminated from the significant list of parameters, with an equivalent elastic modulus used in place of the usual elastic modulus. If the ratio of the cylinder diameter to particle diameter is sufficiently large, i.e., $D_c/D \gg 1$, and the particle number is also sufficiently large $N \gg 1$, then those parameters are expected to play little role in determining the particle internal stress. Lastly,

Table 2
The parameters used in the simulations and their dimensions.

#	Parameter	Dimensions
1	Gravitational acceleration, g	L/T^2
2	Particle length, L	L
3	Particle diameter, D	L
4	Particle density, ρ_p	M/L^3
5	Cylinder diameter, D_c	L
6	Blade height, B	L
7	Impeller rotational speed, ω	$1/T$
8	Fill mass, M_p	M
9	Particle elastic modulus, E_p	$M/(LT^2)$
10	Particle Poisson's ratio, ν_p	–
11	Boundary elastic modulus, E_b	$M/(LT^2)$
12	Boundary Poisson's ratio, ν_b	–
13	Particle-particle sliding friction coefficient, μ_{pp}	–
14	Particle-boundary sliding friction coefficient, μ_{pb}	–
15	Particle-particle coefficient of restitution, ε_{pp}	–
16	Particle-boundary coefficient of restitution, ε_{pb}	–
17	Particle yield strength, σ_Y	$M/(LT^2)$
18	Applied lid stress, σ_{lid}	$M/(LT^2)$
19	Simulation time, t	T

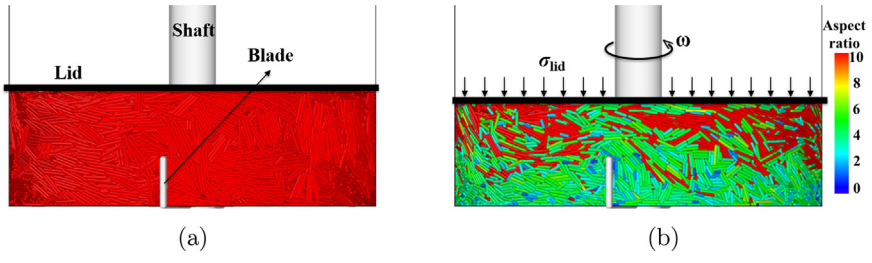

Fig. 8. DEM simulation of needle-shaped, large aspect ratio particle breakage in an agitation cell: (a) agitation cell with mono-disperse particles of aspect ratio 10 before compression and agitation. The agitation cell is comprised of a cylindrical container, an impeller with two flat blades and a central shaft, and an upper lid; (b) particle breakage in the agitation cell after compression and three blade revolutions. The particles are colored according to their aspect ratio, with red corresponding to the maximum aspect ratio and blue the minimum aspect ratio. (For interpretation of the references to colour in this figure legend, the reader is referred to the web version of this article.)

Table 3
List of dimensionless parameters for the simulations.

#	Description	Dimensionless parameter
1	Particle aspect ratio	$AR = L/D$
2	Cylinder-to-particle diameter ratio	D_c/D
3	Blade height-to-cylinder diameter ratio	B/D_c
4	Impeller Froude number	$Fr = \omega^2 D_c/g$
5	Number of particles in the simulation	$N_p = M_p/(c\rho_p g D_p^2 L_p)$, where c = constant
6	Ratio of particle elastic modulus-to-yield strength	E_p/σ_Y
7	Particle Poisson's ratio	ν_p
8	Ratio of boundary-to-particle elastic modulus	E_b/E_p
9	Boundary Poisson's ratio	ν_b
10	Particle-particle sliding friction coefficient	μ_{pp}
11	Particle-boundary sliding friction coefficient	μ_{pb}
12	Particle-particle coefficient of restitution	ε_{pp}
13	Particle-boundary coefficient of restitution	ε_{pb}
14	Ratio of lid force-to-bed weight	$\sigma_{lid} D_c^2/(M_p g)$
15	Ratio of applied lid stress-to-yield strength	σ_{lid}/σ_Y
16	Number of impeller revolutions	$\omega t/(2\pi)$

in the current simulations the blade dimensions, lid stress, and the material properties are held constant in the parametric studies, i.e., $B/D_c, E_p/\sigma_Y, \mu_{pp}, \mu_{pb}, \sigma_{lid} D_c^2/(M_p g)$, and σ_{lid}/σ_Y are all constant. Note that if the simulations involve unbreakable particles, then the number of impeller revolutions will not be a factor at steady state. Thus, for unbreakable particles,

$$\sigma_p/\sigma_Y = f(AR). \tag{8}$$

and for breakable particles,

$$\sigma_p/\sigma_Y = f(AR, \omega t/(2\pi)). \tag{9}$$

These results mean that the dimensionless particle stress depends on the particle aspect ratio regardless of the particle length and diameter, and it will change with the number of impeller revolutions if the particles are allowed to break.

A similar analysis can be performed to investigate the particle aspect ratio, *AR*, dependence on the other parameters. Note that Guo et al. (2017) comprehensively investigated the effect of particle-particle and particle-boundary friction on particle breakage, so these parameters are not taken into account in the current study. For further simplification, the ratio of the boundary-to-particle effective elastic moduli E_b'/E_p' is always equal to one. By simply changing scale and keeping the device geometrically similar, the parameter B/D_c is kept constant through all scales. In a real operations $\sigma_{lid} D_c^2/(M_p g) \gg 1$, which indicates that this dimensionless parameter is likely also not significant. Finally, the aspect ratio distribution depends on,

$$AR = f\left(E_p'/\sigma_Y, \sigma_{lid}/\sigma_Y, \omega t/(2\pi)\right). \tag{10}$$

A sensitivity study has been performed for the dimensionless parameters given in Eq. (10) and the results are presented in the Section 5.

4.1. Dimensionless work done on the particle bed

The mean particle aspect ratio in this study is expressed as a function of the work done on the powder bed by the impeller. This work is equal to $\omega t \tau$ where τ is the impeller torque. It is observed that the impeller torque is linearly proportional to the lid pressure (Guo et al., 2017), σ_{lid}, so that the work done can be expressed as, $k(\omega t \sigma_{lid})$, where k is a proportionality constant. Following the dimensional analysis and prior work (Guo et al., 2017), the work done is made dimensionless by the particle yield strength, σ_Y, so that the dimensionless work done, W , is,

$$W \propto \omega t \sigma_{lid}/\sigma_Y. \tag{11}$$

The mean and the standard deviation of the resulting aspect ratio distribution after breakage is expressed as a function of dimensionless work done and is presented in the following section.

5. Results

The findings from the investigation on particle breakage in the agitation cell are presented in this section. The first subsection presents the temporal evolution of local particle aspect ratio and the location of breakage events. The effect of initial particle aspect ratio on particle stress distributions and the resulting aspect ratio distributions are presented in the second and third subsections. The fourth subsection discusses the effects of various dimensionless parameters, described in Section 4, on the aspect ratio after a long time period. The last subsection presents the daughter particle distributions and specific breakage rates for different parent particle aspect ratios and their implementation in a population balance model.

5.1. Local particle aspect ratio, breakage events regions, and fines generated

A base-case DEM simulation with mono-disperse spherocylinders is performed to study the local particle aspect ratio and breakage events regions. The simulation parameters and material properties used in this simulation are listed in Table 4. Overlapping averaging spherical bins were used to extract data from two elevations in the particle bed, H_{upper} and H_{lower}, shown in Fig. 9a. Note that the field maps are given in the blade's frame of reference so that steady results are obtained.

Fig. 9b shows the local aspect ratio maps at two different elevations after three different blade revolutions. Initially, all of the particles have an aspect ratio of 10, but as time progresses the particles break and the local aspect ratio decreases. Smaller particles appear near the blade due to particle breakage occurring from particle-blade interactions, and at the container base due to the

Table 4
The parameters used in the base-case agitation cell DEM simulation and their values.

Parameter	Values
Particle length, L	20 10^{-3} m
Particle diameter, D	2 10^{-3} m
Particle aspect ratio, $AR = L/D$	10
Particle density, ρ_p	1384.3 kg/m^3
Cylinder diameter, D_c	0.20 m
Blade height, B	25 10^{-3} m
Shaft diameter, D_{shaft}	20 10^{-3} m
Particle elastic modulus, E_p	1.0 10^6 Pa
Particle Poisson's ratio, ν_p	0.30
Boundary elastic modulus, E_b	1.0 10^6 Pa
Boundary Poisson's ratio, ν_b	0.30
Particle-particle sliding friction coefficient, μ_{pp}	0.11
Particle-cylindrical boundary sliding friction coefficient, μ_{pc}	0.171
Particle-impeller boundary sliding friction coefficient, μ_{pi}	0.16
Particle-flat boundary sliding friction coefficient, μ_{pf}	0.45
Particle-particle coefficient of restitution, ε_{pp}	0.6
Particle-boundary coefficient of restitution, ε_{pb}	0.6
Particle yield strength, σ_Y	5.0 10^5 Pa
Particle number, N_p	16,200

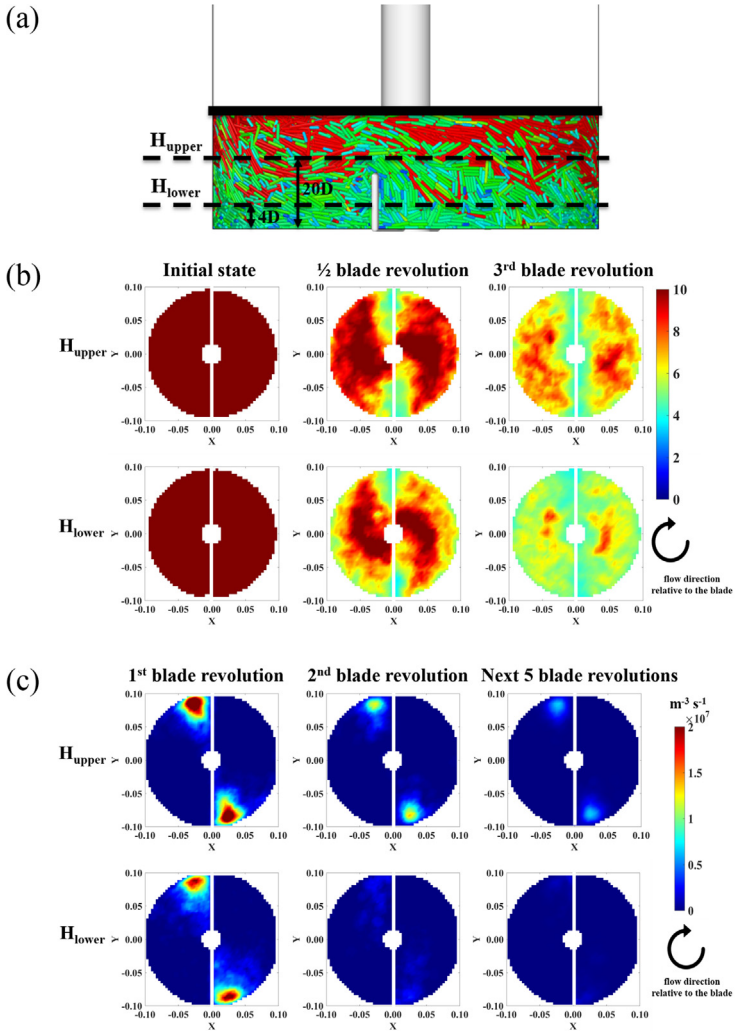

Fig. 9. Two-dimensional surface maps taken from two elevations in the particle bed: (a) the two elevations in the particle bed, H_{upper} and H_{lower}, from which the map data are extracted. H_{upper} is 20*D* above the base and H_{lower} is 4*D* above the base; (b) maps showing particle local aspect ratio fields for the two elevations after three different blade revolutions; (c) maps showing particle breakage events per unit time per unit volume for the two elevations after three different blade revolutions.

small, out-of-plane velocity of particles at the lower elevation (Hua et al., 2013). This result indicates that in a real operation the fines are likely to accumulate near the blade and container base.

The field maps of the number of breakage events per unit time per unit volume are shown in Fig. 9c. Several features are readily apparent from these maps. First, most particle breakage occurs near the blade tips at the circumference of the cylindrical container. This result is consistent with the observations made by Hua et al. (2015) and the high breakage rate near the blade tips is also consistent with the high stress regions identified by Hare et al. (2011). Second, most particle breakage occurs during the first blade revolution and decreases as time increases. Similar observations were made by Remy et al. (2015), in which most of the breakage occurs during the first few blade revolutions and the extent of breakage becomes small after that. In addition, more particle breakage occurs near the upper elevation as compared to the lower one since there is a shear region between the blade tip and the lid, and particles in those regions have a larger probability of breakage. Also, at the lower elevation, the particle breakage almost stops at later times due to the deposition of smaller particles at the container bottom, which need larger stresses to break.

A small amount of fines are generated due to particle breakage and collect near the container base. In a real AFD operation, these fines may hinder incoming dryer air that comes through the AFD base. In this model, the mass of fines generated is related to the mass loss associated with the capping of the sphero-cylinder ends at the breakage plane. The cumulative percent of fines generated with respect to the initial powder mass is expressed as a function of the dimensionless work done on the particle bed and is shown in Fig. 10. The mass fraction of fines generated increases rapidly initially and becomes gradual as the number of blade revolutions progresses. This trend is due to the fact that most of the particle breakage happens during the first blade revolution and then the number of breakage events decreases with time.

5.2. Influence of particle aspect ratio on particle stress

In this study, the particle stress refers to the maximum absolute principal stress, which is observed to occur along the particle circumference at the mid-plane of the particle (Hua et al., 2015). The detailed calculation of maximum absolute principal stress for a sphero-cylindrical particle can be found in Hua et al. (2015). The material properties and geometric parameters for these simulations are the same as those listed in Table 4. In addition, different

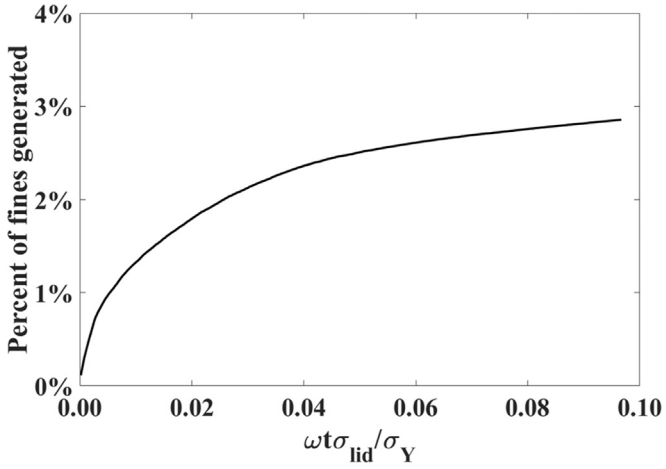

Fig. 10. Cumulative percent of fines generated (by mass) due to particle breakage expressed as a function of dimensionless work done on the particle bed.

combinations of particle length and diameter are also used for the stress calculations. The stress distributions are calculated for both the unbreakable and breakable particles.

The dimensionless time-averaged, steady-state particle stress distributions for the unbreakable particles are given in Fig. 11a. The stress distributions are calculated for four particle aspect ratios (AR = 4, 6, 8, 10) with different combinations of particle length and diameter for each aspect ratio, as given in Table 5. The time averaging is done over three blade revolutions after steady state is attained, which normally occurs after two blade revolutions. Two important observations can be made from this plot: (i) the stress distributions for a given particle aspect ratio are identical regardless of the particle length and diameter, as expected from the dimensional analysis section (Section 4, Eq. (8)); and (ii) the stress values decrease with the particle aspect ratio as shorter particles have a smaller moment arm for generating internal stresses.

For the breakable particles, particle stress depends on the particle aspect ratio as well as the number of blade revolutions. Fig. 11b plots the transient particle stress distributions for an initial aspect ratio of 10 with three different particle length and diameter combinations (Table 5) after four different numbers of blade revolutions. This plot shows that for a given particle aspect ratio, the stress distributions are identical to each other regardless of the particle length and diameter at different simulation times, as expected from the dimensional analysis section (Section 4, Eq. (9)), and the stresses decrease as the particle mean aspect ratio decreases with the number of blade revolutions. The shorter particles result in smaller internal stresses because the moment arm

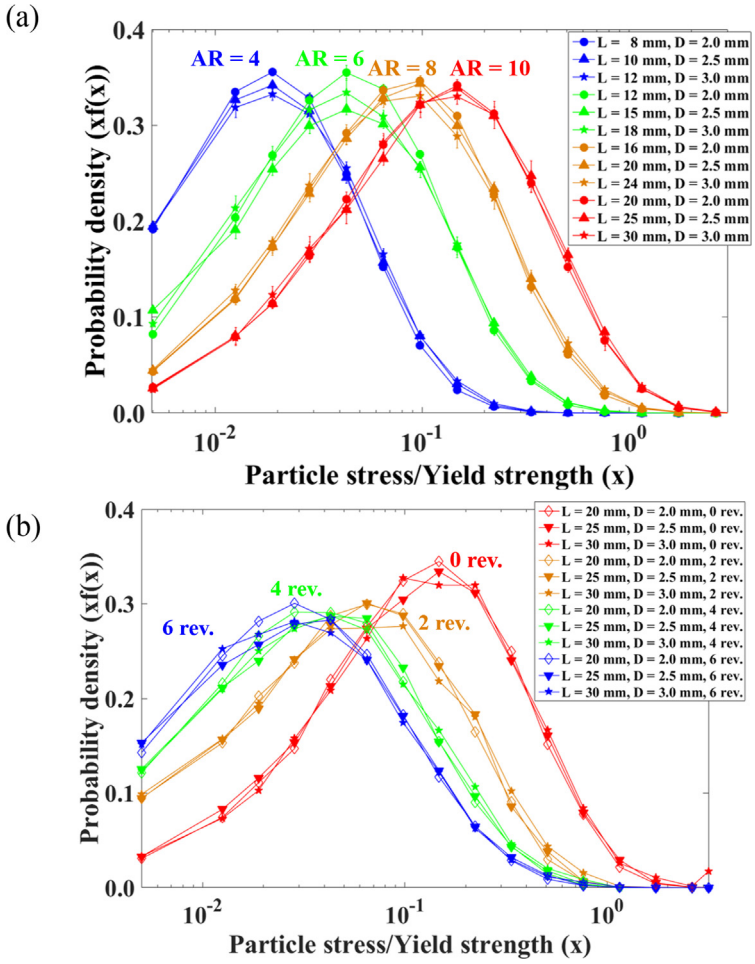

Fig. 11. (a) Dimensionless time-averaged particle stress distributions for unbreakable particles using four different particle aspect ratios (AR = 4, 6, 8, 10) with three different combinations of particle length and diameter for each aspect ratio. The scatter bars represent one standard deviation for data averaged over three blade revolutions; (b) transient dimensionless particle stress distributions for breakable particles using an initial AR = 10 with different particle length and diameter combinations, at four different numbers of blade revolutions.

Table 5
Different combinations of particle length and diameter for the four different particle aspect ratios used in the unbreakable particle stress simulations.

Aspect ratio	Length (m)	Diameter (m)
4	8 10^{-3}, 10 10^{-3}, 12 10^{-3}	2.0 10^{-3}, 2.5 10^{-3}, 3.0 10^{-3}
6	12 10^{-3}, 15 10^{-3}, 18 10^{-3}	2.0 10^{-3}, 2.5 10^{-3}, 3.0 10^{-3}
8	16 10^{-3}, 20 10^{-3}, 24 10^{-3}	2.0 10^{-3}, 2.5 10^{-3}, 3.0 10^{-3}
10	20 10^{-3}, 25 10^{-3}, 30 10^{-3}	2.0 10^{-3}, 2.5 10^{-3}, 3.0 10^{-3}

becomes shorter, which is consistent with the observations made by Hua et al. (2015).

These particle stress plots not only provide confidence in the dimensional analysis, but are also significant from a DEM modeling point of view. A smaller number of larger particles can be used to examine the stress behavior of shorter particles with the same aspect ratio, which can be used to reduce the simulation computational time.

5.3. Influence of initial particle aspect ratio characteristics

This section examines the effects of the initial particle aspect ratio distribution on the evolution of the particle aspect ratio distribution as work is done on the particle bed. The material properties and geometric parameters for these simulations are same as those listed in Table 4. In addition, a combination of particle length and diameter are used to give the same particle aspect ratio. Four different scenarios for initial particle aspect ratio characteristics are investigated here: (i) mono-disperse particles with different combinations of length and diameter, but a constant aspect ratio (AR = 10); (ii) mono-disperse particles with three different aspect ratios (AR = 6, 8, 10); (iii) poly-disperse particles utilizing Gaussian distributions with three different means (AR mean = 8, 10, 12) and a constant standard deviation (AR std. dev. = 2); (iv) polydisperse particles utilizing Gaussian distributions with three different standard deviations (AR std.dev. = 1.0, 1.5, 2.0) and a constant mean (AR mean = 10).

Due to particle breakage, the mean aspect ratio decreases as the number of blade revolutions progresses. Fig. 12a and b plot the mean and standard deviation of the aspect ratio distribution,

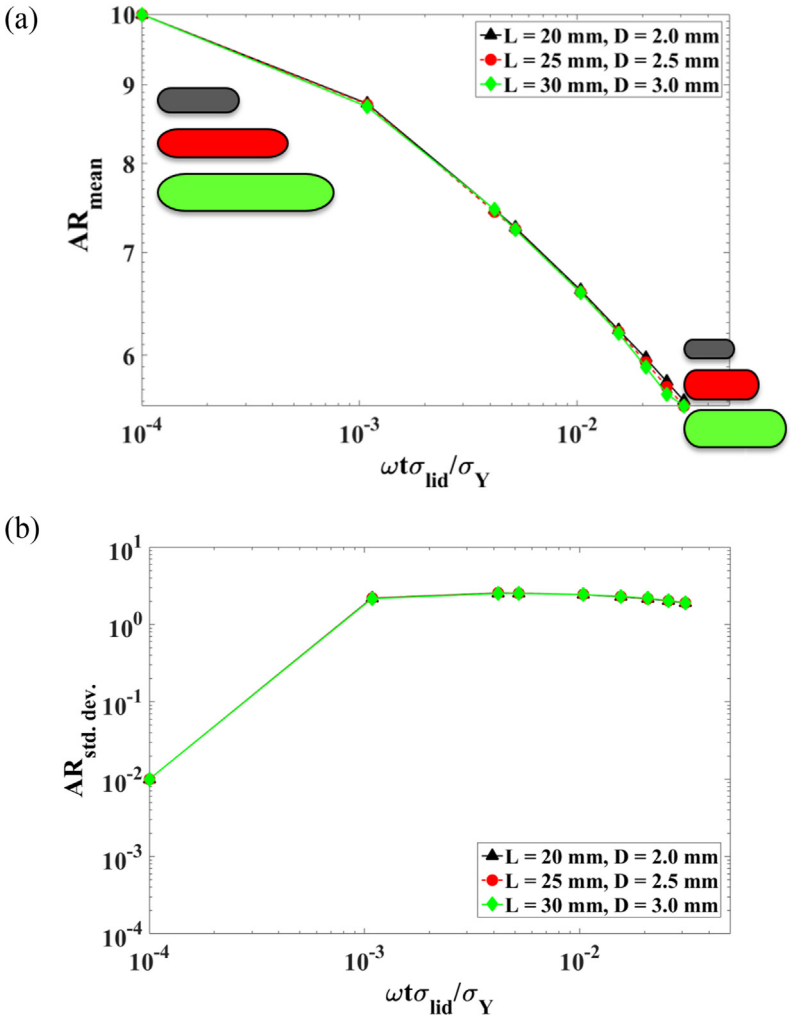

Fig. 12. Particle aspect ratio distribution characteristics for three different combinations of particle length (L = 20 mm, 25 mm, 30 mm) and diameter (D = 2.0 mm, 2.5 mm, 3.0 mm) but the same aspect ratio (AR = 10): (a) particle mean aspect ratio, with cartoons depicting the particle aspect ratio at the initial and the final state; (b) particle aspect ratio standard deviation, expressed as a function of dimensionless work.

respectively, for the first scenario. These plots reveal that both the mean and the standard deviation of the resulting particle aspect ratio distribution are identical to each other for the same initial particle aspect ratio, regardless of the length and diameter combination. For the second scenario in which there are different initial aspect ratio particles, the means and standard deviations of the resulting particle aspect ratio distribution are different initially, but eventually collapse onto each other after a sufficiently large number of blade revolutions. These observations, illustrated in Fig. 13a and b, show that the resulting particle aspect ratio characteristics are independent of the initial particle aspect ratio if enough work is done on particles. Similar observations are made for the third and fourth scenarios in which, instead of monodisperse particles, poly-disperse particles utilizing Gaussian distributions with different initial aspect ratio means and standard deviations are used. For brevity, the mean aspect ratio and standard deviation plots are not shown here, but instead the initial and the resulting aspect ratio distributions after ten blade revolutions are shown. Fig. 14a shows three different initial aspect ratio distributions with different means, but the same standard deviations. Fig. 14b shows three different initial aspect ratio distributions with different standard deviations, but the same mean values. It is clear from these plots that the final particle aspect ratio distributions are identical to each other regardless of the initial particle aspect ratio distribution. These observations are consistent with the findings of Remy et al. (2015), in which they started with two different initial particle size distributions in two different, but geometrically similar agitated systems, and obtained similar final particle size distributions. The final particle aspect ratio distributions are also fit well with a log-normal distribution.

5.4. Influence of particle elastic modulus, lid stress, yield strength, and impeller angular speed on the resulting particle mean aspect ratio

To study the impact of particle elastic modulus (E_p), lid stress (σ_{lid}), and yield strength (σ_Y), the results are expressed in terms of the dimensionless parameters E_p/σ_Y and σ_{lid}/σ_Y. Note that, when one dimensionless parameter is varied, all of the other dimensionless parameters are kept constant. The simulation parameters and material properties are listed in Table 4. Fig. 15 shows the impact of E_p/σ_Y on the resulting particle mean aspect ratio. It is observed that the particle aspect ratio decreases with an increase in E_p/σ_Y. Particle stresses increase with increasing elastic modulus (Hua et al., 2015) causing more breakage. Similarly, if the particle yield strength is reduced, a particle is more likely to break, even under smaller stresses. The impact of the ratio of the lid stress to the particle yield strength on particle mean aspect ratio is shown in Fig. 16. It is observed that the particle mean aspect ratio decreases with an increase in σ_{lid}/σ_Y. In a real operation, if there is more overlying material or particles are more

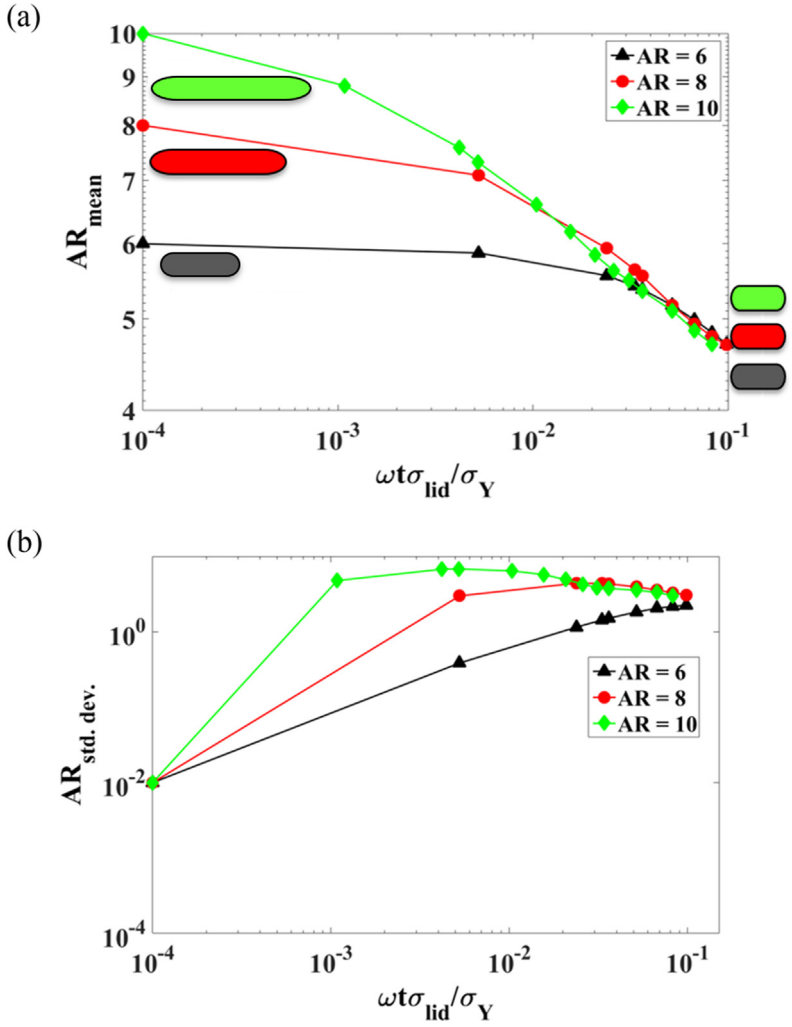

Fig. 13. Particle aspect ratio distribution characteristics for three different initial particle aspect ratios (AR = 6, 8, 10): (a) particle mean aspect ratio, with cartoons depicting the particle aspect ratio at the initial and the final state; (b) particle aspect ratio standard deviation, expressed as a function of dimensionless work.

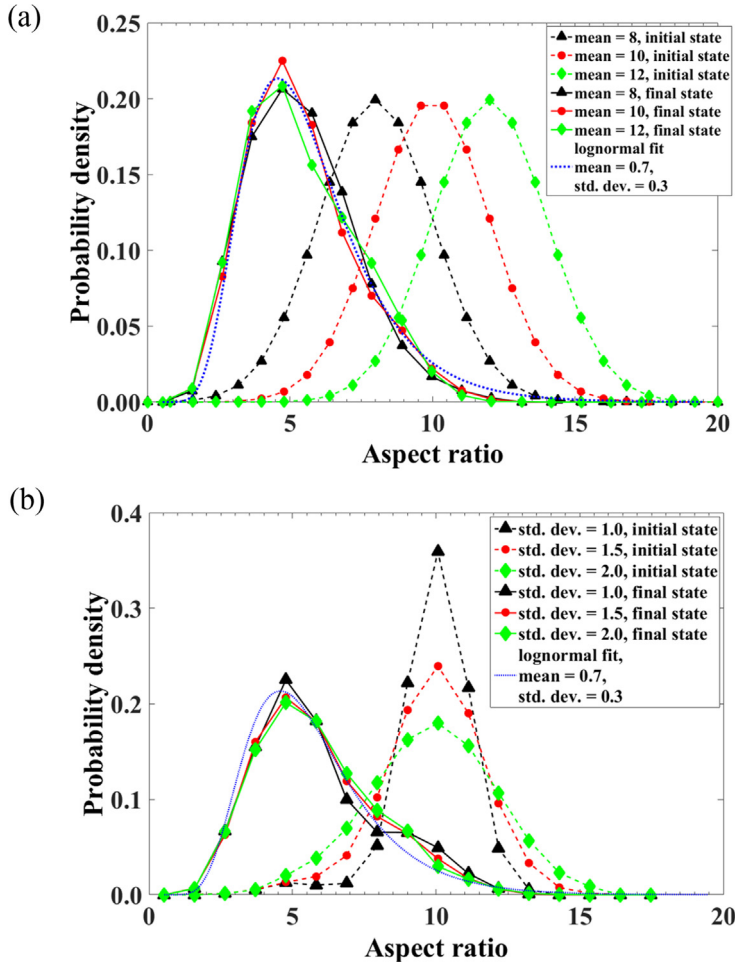

Fig. 14. Particle aspect ratio distributions for different initial particle aspect ratio distributions, with a log-normal fit for the particle aspect ratio distributions represented by a blue dotted line: (a) three initial particle aspect ratio distributions with means of AR = 8, 10, and 12 and a standard deviation of AR = 2 collapsing over a single curve after 10 blade revolutions; (b) three initial particle aspect ratio distributions with standard deviations of AR = 1.0, 1.5, and 2.0 and a mean of AR = 10 collapsing over a single curve after 10 blade revolutions.

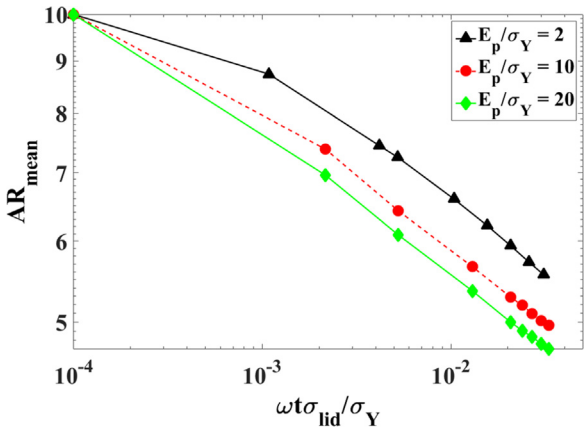

Fig. 15. Particle mean aspect ratio expressed as a function of dimensionless work for three different E_p/σ_Y ratios of 2, 10, and 20.

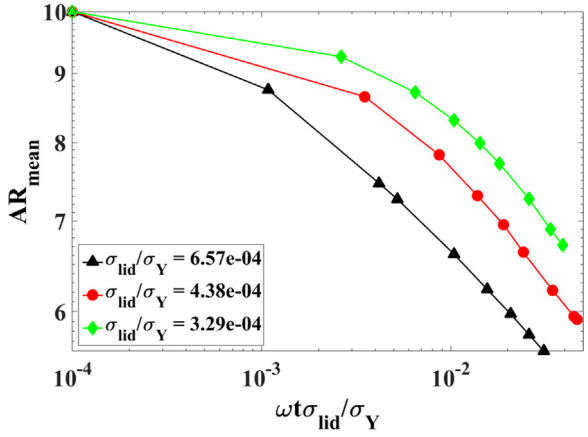

Fig. 16. Particle mean aspect ratio expressed as a function of dimensionless work for three different σ_{lid}/σ_Y ratios of 6.57 10 ^{4}, 4.38 10 ^{4}, and 3.29 10 ^{4}.

friable, then there will be more breakage, as expected. Another important observation from Figs. 15 and 16 is that the slope of all of the curves are generally constant. It may be possible to develop correlations for the influence of these dimensionless parameters if a wider range of values is considered.

Fig. 17 demonstrates the influence of impeller rotational speed on the resulting particle mean aspect ratio expressed as a function of amount of work done on the particle bed. It is found that the extent of breakage per impeller revolution is independent of the impeller rotational speed. This result means that the extent of par-

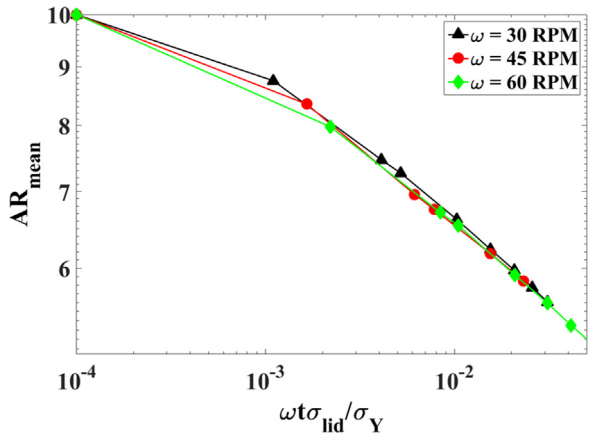

Fig. 17. Particle mean aspect ratio expressed as a function of dimensionless work for three different blade rotational speeds (ω = 30 RPM, 45 RPM, and 60 RPM).

ticle breakage, at least over the rotation speeds investigated, is a function of blade displacement or the work done rather than the rotational speed, a result that has also been observed by Hare et al. (2011), Remy et al. (2015) and Guo et al. (2017). Note that at larger impeller rotational speeds, the stresses are anticipated to be a function of the impeller speed, with breakage rate increasing with impeller speed. However, in practice, agitated filter drying operations typically operate at low impeller speeds.

5.5. Particle specific breakage rates, daughter particle distribution functions, and population balance modeling

The particle specific breakage rates and daughter particle length distributions are the two parameters required for population balance model predictions. These parameters are obtained from the DEM simulations, for which the simulation parameters and material properties are provided in Table 4. In addition, a Gaussian distribution, with an AR mean of 12 and an AR standard deviation of two, is used for the initial aspect ratio distribution. Note that the particle breakage is always binary, i.e., one parent particle always breaks into two daughter particles.

To be able to utilize the breakage rate information in a population balance model, it is important to derive a general breakage rate function based on the DEM breakage rates. This function can not only be used to predict the particle size distribution for extended time periods, but also for large-scale systems for which running a DEM simulation may not be computationally feasible. The dimensionless specific breakage rate, S_i, is expressed as,

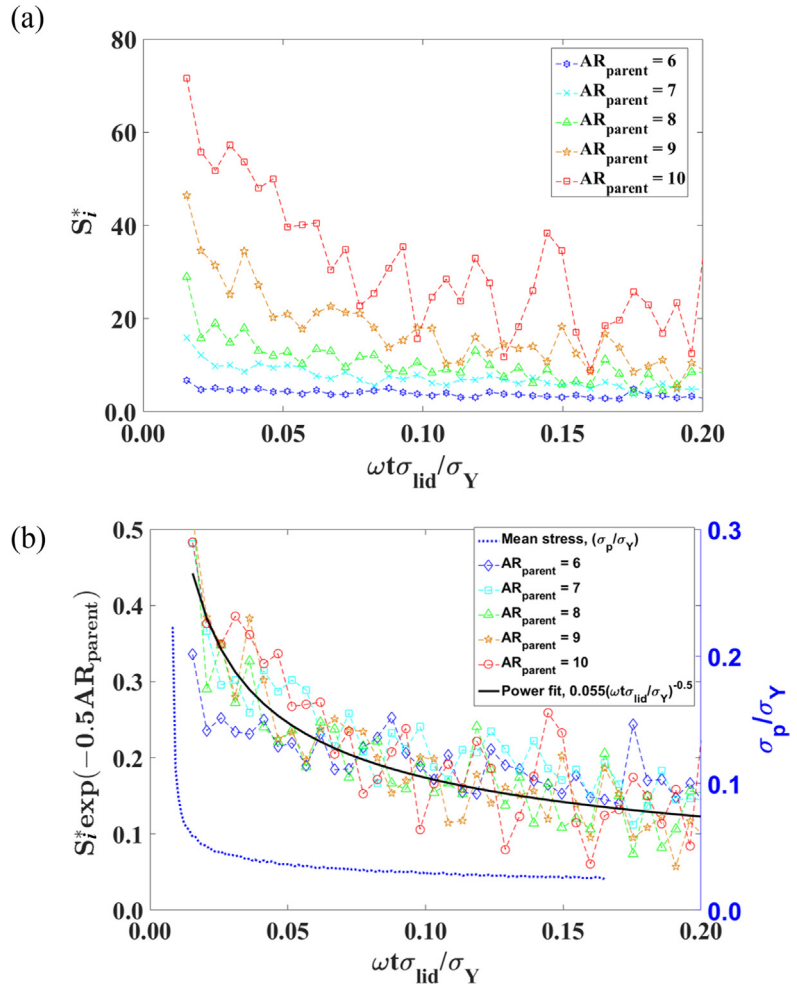

Fig. 18. Dimensionless specific particle breakage rates (S_i) expressed as a function of dimensionless work done for five different parent particle aspect ratios (AR = 6, 7, 8, 9, 10): (a) Unscaled dimensionless specific particle breakage rates; (b) dimensionless specific breakage rates scaled using an exponential function ($\exp(-0.5AR_{parent})$) and fitted with a power curve ($0.055(\omega t\sigma_{lid}/\sigma_Y)^{-0.5}$) depicted on the left y-axis. Mean dimensionless particle stress (σ_p/σ_Y) denoted by a dotted blue curve depicted on the right y-axis. (For interpretation of the references to colour in this figure legend, the reader is referred to the web version of this article.)

$$S_i = \frac{\Delta N_i}{N_i \omega \Delta t (\sigma_{lid}/\sigma_Y)} \quad (12)$$

where N_i is the number of particles of aspect ratio *i*. The breakage rate is normalized here by the dimensionless work rather than time. Fig. 18a plots S_i for five different parent aspect ratios (AR_{parent} = 6, 7, 8, 9, 10). It can be observed that the dimensionless specific breakage rate increases with parent aspect ratio indicating that larger aspect ratio particles have a greater tendency to break. The breakage rate curves are noisy due to the limitation of using a smaller number of particles in the DEM simulation compared to a real system. The breakage curves for different parent aspect ratios are scaled by multiplying an (empirically-determined) exponential function, $\exp(-0.5AR_{parent})$, to S_i. The scaled breakage rate curves plotted in Fig. 18b collapse reasonably well onto each other and can be fitted with an empirically-determined power function, $0.055(\omega t \sigma_{lid}/\sigma_Y)^{0.5}$. This function is used in the population balance model to predict the particle size distribution. Another observation from Fig. 18a and b is that the slope of the dimensionless breakage rate is initially large, then becomes increasingly smaller as the number of blade revolutions increases. This change is attributed to the decrease in the particle stresses in the particle bed, which changes rapidly initially but slows down after some time as there are more particles in the system after breakage to share the load and the particle sizes are smaller. The particle stress is represented by the dotted blue curve in the Fig. 18b.

The influence of the initial particle aspect ratio on the specific breakage rate is also investigated. Fig. 19a plots the scaled dimensionless specific breakage rate as a function of system mean aspect ratio (AR_{mean}) for three different initial particle aspect ratio distribution means (AR mean = 8, 10, 12) and an AR standard deviation of 2.0, with three parent aspect ratios (AR_{parent} = 6, 8, 10) for each mean. Fig. 19b shows the scaled dimensionless specific breakage rate as a function of system mean aspect ratio for three different initial particle aspect ratio distribution standard deviations (AR std. dev. = 1.0, 1.5, 2.0) and a mean of AR = 10, with three parent aspect ratios (AR_{parent} = 6, 8, 10) for each standard deviation. It is observed from these plots that the breakage rates are independent of the initial particle aspect ratio distribution characteristics. At any given time instance, if the mean aspect ratio of the system is known, these plots can be used to obtain the specific breakage rate for different aspect ratio classes. Although not shown here for brevity, the impact of the lid stress, particle yield strength, particle elastic modulus, and blade rotational speed were also investigated. The specific breakage rate increases with an increase in lid stress and particle elastic modulus and with a decrease in particle yield strength and is insensitive to the blade rotational speed at the investigated speeds (30, 45, and 60 RPM).

The daughter particle length distribution functions for different parent particle aspect ratios are shown in Fig. 20. It is observed that the needle-shaped particles always break in a similar way regardless of the parent particle aspect ratio. This self-similarity behavior of the daughter particle length distribution functions leads to the

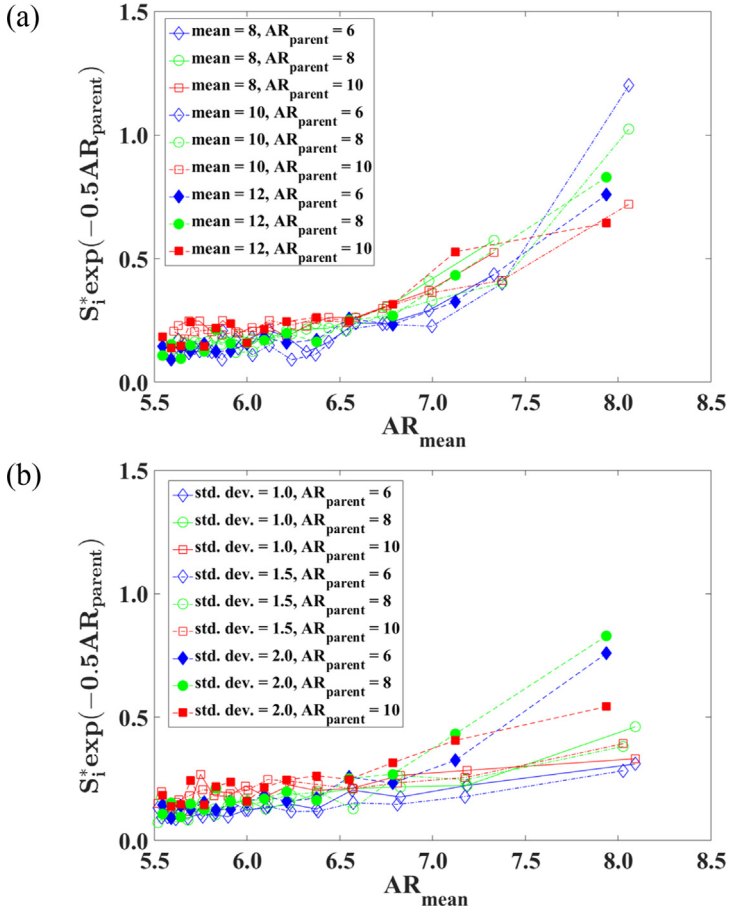

Fig. 19. Scaled dimensionless specific breakage rates ($S_i \exp(-0.5AR_{parent})$) for different initial particle aspect ratios expressed as a function of the system mean aspect ratio (AR_{mean}): (a) plots for three different initial particle aspect ratio distribution means (AR mean = 8, 10, 12) and a constant standard deviation of AR = 2, with three parent aspect ratios for each mean (AR_{parent} = 6, 8, 10); (b) plots for three different initial particle aspect ratio distribution standard deviations (AR std. dev. = 1.0, 1.5, 2.0) and a constant mean of AR = 10, with three parent aspect ratio for each mean (AR_{parent} = 6, 8, 10).

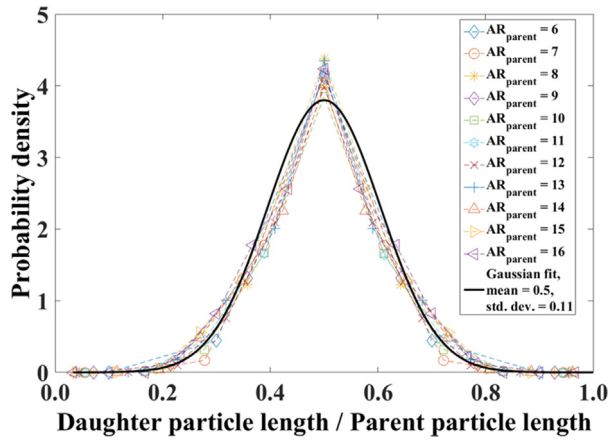

Fig. 20. Plots of daughter particle length distributions normalized by the parent particle length for different parent particle aspect ratios and fitted by a Gaussian function with mean = 0.5 and std. dev. = 0.11.

collapse of all of the functions into one universal distribution, which can be fitted by a Gaussian distribution with a mean of 0.5 and standard deviation of 0.11. A similar observation for the daughter distribution function was made by Grof et al. (2011) for needle-shaped particle breakage under compaction. The daughter particle length distribution functions are also found to be insensitive to the material properties and operating conditions. The main advantage of the self-similar behavior of the daughter particle length distribution functions is that a single small-scale DEM simulation can be used to generate these functions, which can then be used to predict particle breakage in a large-scale system.

The specific breakage rate and the daughter particle distribution functions derived from the DEM simulation are used in a population balance model (PBM) to predict particle breakage in an agitation cell. Comparisons between the PBM and DEM particle aspect ratio distributions are shown in Fig. 21a. The PBM predictions match well with the DEM results, which is expected since the PBM specific breakage rate and daughter size distribution are fit from the DEM data. The advantage of the PBM is that it can be used to predict the particle size distributions for extended time periods that are time consuming to model with DEM, as can be seen in Fig. 21b. Interestingly, the particle aspect ratio distribution at extended times is fit well using a log-normal distribution expressed as,

$$f(x,a,b) = \frac{1}{xb\sqrt{2\pi}} \exp\left(\frac{-(ln(x)-a)^2}{2b^2}\right) \quad (13)$$

where a and b are two parameters that are functions of the mean and variance of the distribution (Weisstein, 1999), with values of 3.60 and 0.30, respectively, at a simulation time of 750 s.

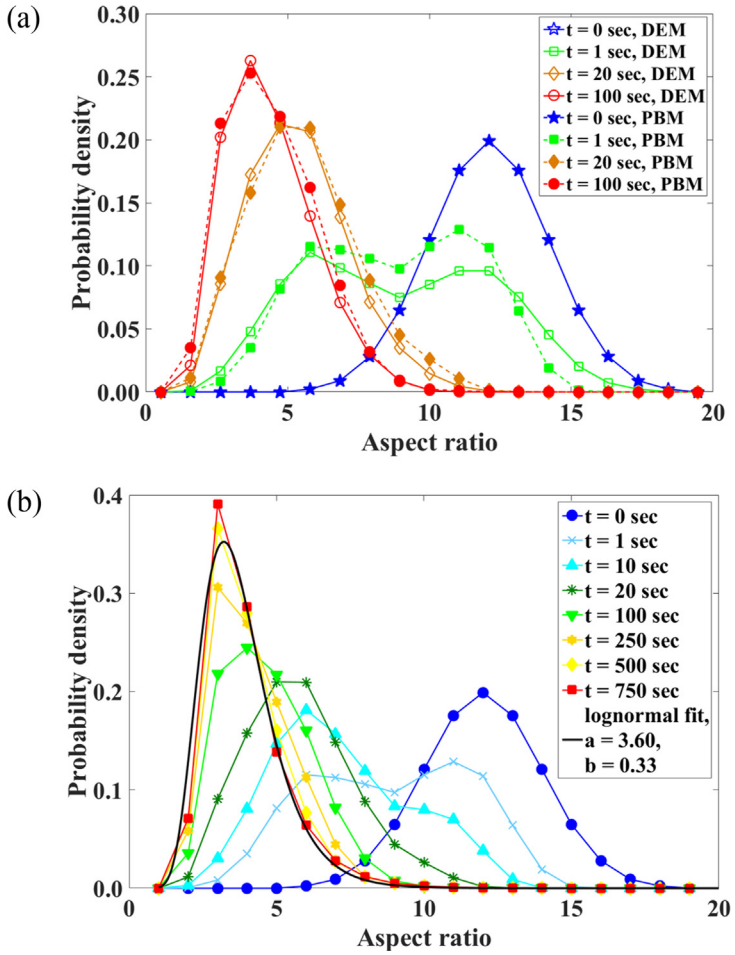

Fig. 21. Population balance modeling results: (a) comparison between the DEM and the PBM predicted particle aspect ratio distributions for four different time instances; (b) particle aspect distribution predictions for extended time periods utilizing the PBM, with a log-normal fit for the resulting particle aspect ratio distribution at t = 750 s.

6. Conclusions

This work presents a novel, experimentally-validated DEM model for investigating the breakage of large aspect ratio particles. What separates the current DEM model from previous ones are that a breakable sphero-cylinder particle model is used so that the change in breakage rates could be investigated during a simulation. In addition, parametric studies were performed to investigate the effects of particle properties (elastic modulus, yield strength, initial size distribution) and operating conditions (lid stress, impeller speed).

Several interesting results were observed. First, the particle aspect ratio distribution is independent of the initial aspect ratio distribution after sufficient work is done on the particle bed. In addition, this final aspect ratio distribution is fit well with a log-normal distribution. Increasing the ratio of the particle elastic modulus to yield strength and the lid stress to yield strength act to increase the rate of breakage. Changing impeller speed has little influence, at least over the range of speeds investigated here.

Another contribution of the work is that the DEM model was used to determine dimensionless specific breakage rate and daughter distribution functions that were used in a population balance model. Unlike many PB models, the specific breakage rate is not treated as a constant here since the particle size distribution, and thus stress field, within the system changes with time. Predictions from the population balance model were used to investigate the long-term behavior of the system. As expected, the aspect ratio distribution is independent of the initial aspect ratio distribution and has a form that is fit well with a log-normal distribution. As work on the bed increases, the mean and standard deviation of the log-normal function decreases, with the standard deviation decreasing more rapidly than the mean.

Future work should investigate how the specific breakage rate expression derived for the current attrition cell changes with scale. It is likely that the daughter size distribution remains the same, but the specific breakage rate likely changes because the stress field in the bed is likely to change. Although the constants in the specific breakage rate expression are expected to change, it would be useful to know if the form of the fit is still applicable.

Declaration of Competing Interest

The authors declared that there is no conflict of interest.

References

AmEnde, D., Maloney, M.T., Birch, M., Brenek, S.J., 2013. Development and application of laboratory tools to predict particle properties upon scale-up in Agitated Filter-Dryers Agitated Filter Dryers (AFDs). Org. Process Res. Dev. 17, 1345–1358.

Freireich, B., Litster, J., Wassgren, C., 2009. Using the discrete element method to predict collision-scale behavior: a sensitivity analysis. Chem. Eng. Sci. 64, 3407–3416.

Ghadiri, M., Ning, Z., Kenter, S.J., Puik, E., 2000. Attrition of granular solids in a shear cell. Chem. Eng. Sci. 55, 5445–5456.

Grof, Z., Kohout, M., Stepanek, F., 2007. Multi-scale simulation of needle-shaped particle breakage under uniaxial compaction. Chem. Eng. Sci. 62, 1418.

Grof, Z., Schoellhammer, C.M., Rajniak, P., Štepánek, F., 2011. Computational and experimental investigation of needle-shaped crystal breakage. Int. J. Pharmaceut. 407, 12–20.

Guo, Y., Wassgren, C., Hancock, B., Ketterhagen, W., Curtis, J., 2017. Predicting breakage of high aspect ratio particles in an agitated bed using the Discrete Element Method. Chem. Eng. Sci. 158, 314–327.

Guo, Y., Wassgren, C., Ketterhagen, W., Hancock, B., James, B., Curtis, J., 2012. A numerical study of granular shear flows of rod-like particles using the discrete element method. J. Fluid Mech. 713, 1–26.

Hare, C., Ghadiri, M., Dennehy, R., 2011. Prediction of attrition in agitated particle beds. Chem. Eng. Sci. 66, 4757–4770.

Hibbeler, R.C., 2005. Mechanics of Materials. Prentice Hall, Singapore.

Hua, X., Curtis, J., Guo, Y., Hancock, B., Ketterhagen, W., Wassgren, C., 2015. The internal loads, moments, and stresses in rod-like particles in a low-speed, vertical axis mixer. Chem. Eng. Sci. 134, 581–598.

Hua, X., Curtis, J., Hancock, B., Ketterhagen, W., Wassgren, C., 2013. The kinematics of non-cohesive, sphero-cylindrical particles in a low-speed, vertical axis mixer. Chem. Eng. Sci. 101, 144–164.

Johnson, K.L., 1985. Contact Mechanics. Cambridge University Press, Cambridge, United Kingdom.

Kodam, M., Bharadwaj, R., Curtis, J., Hancock, B., Wassgren, C., 2009. Force model considerations for glued-sphere discrete element method simulations. Chem. Eng. Sci. 64, 3466–3475.

Kumar, R., Sarkar, A., Ketterhagen, W., Hancock, B., Curtis, J., Wassgren, C., 2018. Influence of normal contact force model on simulations of spherocylindrical particles. AIChE J. 64, 1986–2001.

Lamberto, D.J., Cohen, B., Marencic, J., Miranda, C., Petrova, R., Sierra, L., 2011. Laboratory methods for assessing API sensitivity to mechanical stress during agitated drying. Chem. Eng. Sci. 66, 3868–3875.

Langston, P., Kennedy, A.R., Constantin, H., 2015. Discrete element modelling of flexible fibre packing. Comput. Mater. Sci. 96, 108–116.

Lekhal, A., Girard, K.P., Brown, M.A., Kiang, S., Glasser, B.J., Khinast, J.G., 2003. Impact of agitated drying on crystal morphology: KCl-water system. Powder Technol. 132, 119–130.

Lekhal, A., Girard, K.P., Brown, M.A., Kiang, S., Khinast, J.G., Glasser, B.J., 2004. The effect of agitated drying on the morphology of L-threonine (needle-like) crystals. Int. J. Pharmaceut. 270, 263–277.

MacLeod, C.S., Muller, F.L., 2012. On the fracture of pharmaceutical needle-shaped crystals during pressure filtration: case studies and mechanistic understanding. Org. Process Res. Dev. 16, 425–434.

Mindlin, R.D., Deresiewicz, H., 1953. Elastic spheres in contact under varying oblique forces. Trans. ASME J. Appl. Mech. 20, 327–344.

Nassauer, B., Kuna, M., 2013. Contact forces of polyhedral particles in discrete element method. Gran. Matter 15, 349–355.

Neil, A.U., Bridgwater, J., 1994. Attrition of particulate solids under shear. Powder Technol. 80, 207–219.

Popov, E.P., 1999. Engineering Mechanics of Solids. Prentice Hall, New Jersey, USA.

Potapov, A.V., Campbell, C.S., 1997. Computer simulation of shear-induced particle attrition. Powder Technol. 94, 109–122.

Pournin, L., Weber, M., Tsukahara, M., Ferrez, J.A., Ramaioli, M., Liebling, T.M., 2005. Three-dimensional distinct element simulation of spherocylinder crystallization. Gran. Matter 7, 119–126.

Remy, B., Kightlinger, W., Saurer, E.M., Domagalski, N., Glasser, B.J., 2015. Scale-up of agitated drying: effect of shear stress and hydrostatic pressure on active pharmaceutical ingredient powder properties. AIChE 61, 407–418.

Rhodes, M.J., 2008. Introduction to Particle Technology. Wiley, Chichester, England; Hoboken, NJ.

Sato, K., Nagai, H., Hasegawa, K., Tomori, K., Kramer, H.J.M., Jansens, P.J., 2008. Two-dimensional population balance model with breakage of high aspect ratio crystals for batch crystallization. Chem. Eng. Sci. 63, 3271–3278.

Stukowski, A., 2009. Visualization and analysis of atomistic simulation data with OVITO–the open visualization tool. Model. Simul. Mater. Sci. Eng. 18, 012–015.

Thakur, R.S., Shukla, J.J., Desale, G.R., Ghosh, P.K., 2017. Understanding the factors influencing quality of writing and wiping for chalk and board system. Curr. Sci. 112, 1727–1737.

Thornton, C., Yin, K.K., 1991. Impact of elastic spheres with and without adhesion. Powder Technol. 65, 153–166.

Tsuji, Y., Tanaka, T., Ishida, T., 1992. Lagrangian numerical simulation of plug flow of cohesionless particles in a horizontal pipe. Powder Technol. 71, 239–250.

Weisstein, E.W., 1999. Log Normal Distribution. From MathWorld–A Wolfram Web Resource. <http://mathworld.wolfram.com/LogNormalDistribution.html>.